Acta Mechanica 183, 155–176 (2006)
DOI 10.1007/s00707-006-0313-z

Acta Mechanica
Printed in Austria

Wave propagation generated by piezoelectric actuators attached to elastic substrates

X. D. Wang and **G. L. Huang**, Edmonton, Alberta

Received May 16, 2005; revised November 15, 2005
Published online: April 10, 2006

Summary. Piezoelectric actuators can be used to generate high-frequency elastic waves for damage identification of materials. This paper provides a comprehensive theoretical study of the electromechanical behavior of surface-bonded or embedded piezoelectric actuators under inplane electric fields. A modified one-dimensional actuator model is introduced, from which arbitrarily distributed electric fields along the actuator can be considered. The model is used to simulate the dynamic load transfer between the actuator and the host medium and the resulting elastic wave propagation by using the integral transform method and solving the resulting singular integral equations. Of particular interest is the generated waveform away from the actuator under different electric fields. An asymptotic analysis is conducted to obtain the far-field solution of the wave field. The property of the resulting waveform is studied, and the simulation shows that the direction of wave propagation can be adjusted by controlling the phase distribution of the applied electric field along the actuator.

1 Introduction

The development of new piezoceramic materials with high electromechanical coupling has revived intense research and development of new piezoelectric actuators for different structural applications, e.g., the vibration and noise control of space and aircraft structures, the smart skin system for submarines, smart sports products, and the non-destructive evaluation (NDE) of materials [1]–[4]. These new piezoceramic actuators can be easily fabricated in different desired shapes and can be used in different applications to achieve the highest possible deformation or force for lowest possible applied voltage. They have the advantages of low cost, quick response, low power consumption, compactness, and high sensitivity over a large range of loading frequencies. As a result, in addition to the application in monitoring and controlling the global behavior of structures, they also show the potential to induce high-frequency wave propagation in the host structure for damage identification. Unlike the process of vibration control, damage detection using high-frequency elastic waves usually involves wavelengths comparable to the size of the actuator and, therefore, requires a detailed understanding of the local electromechanical field around the actuator.

Due to the presence of the material discontinuity between the actuators and the host medium, complicated stress fields will be generated when external electric fields are applied to the actuators, which are usually difficult to deal with analytically. Simplified actuator models have been developed to simulate the actuation process. Crawley and de Luis [5] first analyzed a

beam-like structure with surface-bonded and embedded thin-sheet piezoelectric actuators to study the load transfer from the actuators to the host structure. In this analysis, the axial stress in the actuator was assumed to be uniform across its thickness. Crawley and Anderson [6] developed a Bernoulli-Euler model of a piezoelectric actuator by considering the linear stress distribution across the thickness. A refined actuator model based on the plane stress condition was further studied to investigate the electromechanical behavior of a beam with symmetrically surface-bonded actuator patches [7]. Plate and shell models have been extensively used in modelling the electromechanical behavior of piezoelectric structures [8]–[12]. To simulate the actuation process for cases where the size of the actuators is smaller than the thickness of the host structure, Wang and Meguid [13] studied the static behavior of a thin-sheet piezoelectric actuator attached to an infinite elastic medium using a one-dimensional model to investigate the load transfer between the actuator and the host medium and the stress concentration near the ends of the actuator. The static electromechanical field of a piezoelectric layer bonded to an elastic medium with both interfacial and normal stresses being considered has also been studied [14], [15].

Using elastic waves induced by piezoelectric actuators to detect damage in structures has received significant attention from the research community. Many researchers have studied the techniques of generating and collecting diagnostic elastic waves using these actuators to realize continuous monitoring of structures. Distributed piezoelectric ceramic (PZT) disks were used as surface actuators/sensors to generate and receive signals to detect damage in composite structures due to impact [16]. The experimental results showed very promising features of integrated piezoelectric sensor/actuator systems in structural health monitoring. The electro-mechanical impedance method was developed [17] for identifying damage by monitoring the impedance of the structure. This method was used in the health monitoring of thin-wall structures based on the usage of embedded piezoelectric wafer active sensors [18]. The results indicated that the developed electro-mechanical impedance method is suitable for near field damage detection, while guided ultrasonic Lamb waves in conjunction with the pulse-echo technique are suitable for far-field damage detection.

To study the high-frequency dynamic behavior of a piezoelectric thin-sheet actuator with the typical wavelength being comparable to or shorter than the length of the actuator, a one-dimensional model was developed and used to simulate the dynamic actuation process of an embedded actuator [19]. This model was further extended to surface-bonded actuators [20] and to include transverse deformation of the actuator [21]. Since the study was targeted at piezoceramic thin-sheets with electrodes on both sides, the model was limited to the cases where the applied electric field is uniform along the actuator.

The objective of the present paper is to provide a comprehensive analytical study of the wave propagation induced by piezoelectric actuators bonded to or embedded in an elastic medium subjected to different high-frequency electric fields. A modified one-dimensional actuator model, which can simulate arbitrary electric fields along the actuator and contains the effect of both the longitudinal and the transverse deformations of the actuator, is introduced. Numerical simulations were conducted to evaluate the property of the resulting elastic wave propagation. Specifically, two aspects of the work were examined. The first was concerned with the effect of the geometry, material mismatch, loading frequency and especially the distribution of the applied electric field along the actuator. The second was concerned with the property of the resulting waveform at the far-field. An asymptotic analysis was conducted to obtain the explicit analytical solution of the far-field waveform. The numerical result shows that the propagation direction of the resulting wave can be controlled by adjusting the phase distribution of the applied electric field along the actuator.

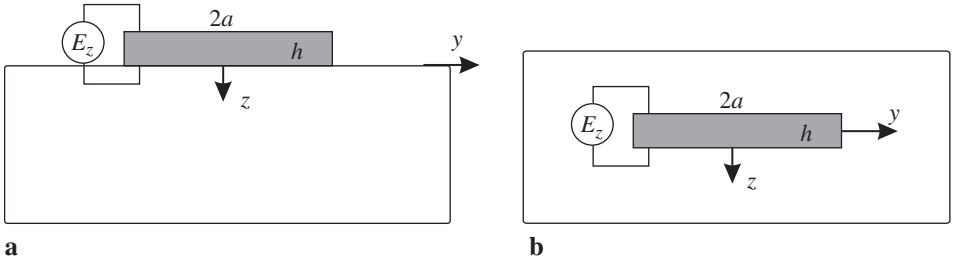

Fig. 1. Surface-bonded and embedded actuators

2 Formulation of the problem

Consider the plane strain problem of piezoelectric actuators surface-bonded to or embedded in homogeneous and isotropic elastic planes, as illustrated in Fig. 1. The actuators considered are piezoelectric elements in the form of thin sheets. For these elements, the so-called poling direction is usually along the thickness to enhance the actuating/sensing effect. For the current problem, the poling direction of the sensor is assumed to be in the direction of the z-axis. The half length and the thickness of the actuator are denoted as a and h, respectively. The actuator is subjected to an applied electric voltage across its thickness, which varies along the actuator and results in an electric field with a frequency ω along the poling direction, $E_z = (V^- - V^+)/h$, as shown in Fig. 1. The steady-state response of the system, including the displacement, strain, stress and electric fields, will generally involve a time factor $\exp(-i\omega t)$. In the following discussion, for convenience, this factor will be suppressed and only the amplitudes of the electromechanical field will be considered.

2.1 Modelling of the actuator

For a thin-sheet piezoelectric actuator, when its thickness being small in comparison with its length and the typical wave length of the generated elastic wave, the axial stress and deformation can be assumed to be uniform across its thickness. The actuator can then be regarded as a one-dimensional electromechanical element deformed in both longitudinal and transverse directions. The interfacial normal and shear stresses transferred between the actuator and the host medium can be replaced by distributed body forces acting along the actuator, as shown in Fig. 2, in which τ and σ_z represent the shear and normal stresses, respectively. For a surface-bonded thin-sheet actuator, the transverse interfacial stress between the actuator and the host medium can be ignored since the actuator is under the traction free condition at the upper surface.

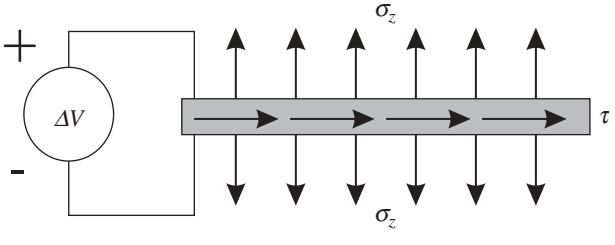

Fig. 2. A one-dimensional actuator model

The current study will be focussed on the case where high-frequency electric fields are applied to the actuator, which result in elastic waves in the host medium with their typical wave length being comparable to the length of the actuator. Therefore, the inertia effect of the actuator must be considered in the modelling of the actuator. Based on the assumptions discussed above, the equation of motion of the actuator along the axial direction can be expressed as

$$\frac{d\varepsilon_y^a}{dy} + \tau/h + \rho_a \omega^2 u_y^a = 0, \tag{1}$$

where ρ_a is the mass density of the actuator. Making use of the constitutive relation of the actuator given in Appendix A, the axial deformation (strain) of the actuator can be obtained by solving this ordinary differential equation, which can be expressed in terms of the applied electric field, the interfacial stress and the transverse deformation of the actuator as

$$\varepsilon_y^a(y) = \varepsilon_0(y) - \int_{-a}^{y} \cos k_a(\xi - y)\frac{p(\xi)}{hE_a}d\xi + \frac{\sin k_a(a+y)}{hE_a \sin 2k_a a}\int_{-a}^{a} \cos k_a(\xi - a)p(\xi)d\xi, \tag{2}$$

where

$$\varepsilon_0(y) = \frac{e_a}{2E_a}\left\{[E_z(a) + E_z(-a)]\frac{\cos k_a y}{\cos k_a a} + [E_z(a) - E_z(-a)]\frac{\sin k_a y}{\sin k_a a}\right\}, \tag{3}$$

$$p(y) = \begin{cases} \tau(y) + hE'_a \dfrac{d\varepsilon_z^a}{dy} - he_a \dfrac{dE_z(y)}{dy} & \text{embedded} \\ \tau(y) - he_a \dfrac{dE_z(y)}{dy} & \text{surface-bonded,} \end{cases}$$

where ε_z^a is the transverse strain given by

$$\varepsilon_z^a = (u_z^{a+} - u_z^{a-})/h \tag{4}$$

with u_z^{a+}, u_z^{a-} being the transverse displacements at the upper and lower surfaces of the actuator. In these equations, E_a, E'_a and e_a are effective elastic and piezoelectric constants of the actuator given in Appendix A, and

$$k_a = \omega/c_a, \quad c_a = \sqrt{E_a/\rho_a} \tag{5}$$

with k_a and c_a being the wave number and the axial wave speed of the actuator, respectively. The transverse normal stress of the actuator, σ_z^a, can be determined using the constitutive relation as

$$\sigma_z^a(y) = \begin{cases} c_{31}^a \varepsilon_0(y) + \dfrac{c_{31}^a \sin k_a(a+y)}{hc_{11}^a \sin 2k_a a}\displaystyle\int_{-a}^{a} p(\xi)\cos k_a(\xi - a)d\xi \\ \quad -\dfrac{c_{31}^a}{hc_{11}^a}\displaystyle\int_{-a}^{y} p(\xi)\cos k_a(\xi - y)d\xi + c_{33}^a \varepsilon_z^a - e_{33}^a E_z(y) & \text{embedded} \\ 0 & \text{surface-bonded,} \end{cases} \tag{6}$$

where c_{11}^a, c_{31}^a, c_{33}^a and e_{33}^a are elastic and piezoelectric constants of the actuator defined in Appendix A.

The interfacial shear stress τ and the transverse deformation ε_z^a of the actuator will deform the host medium and result in elastic wave propagation. Since the actuator is integrated into the host medium, to determine τ and ε_z^a, the coupling between the actuator and the host medium must be considered.

The stress and displacement fields of the host medium can be represented in terms of τ and ε_z^a by solving an elastodynamic problem with τ and ε_z^a being regarded as the applied boundary load and deformation. For convenience, the derivative of ε_z^a with respect to y will be used in the following discussion and is denoted as

$$\phi(y) = \frac{d\varepsilon_z^a}{dy}. \tag{7}$$

By using the Fourier transform with respect to y, which is defined as

$$\overline{g}(s) = \int_{-\infty}^{\infty} g(x)e^{isy}dy, \quad g(y) = \frac{1}{2\pi}\int_{-\infty}^{\infty} \overline{g}(s)e^{-isy}ds, \tag{8}$$

this problem can be solved and the dynamic stress and strain fields in the host medium induced by the applied τ and ε_z^a can be determined,

$$\varepsilon_y(y,0)|_{matrix} = -\frac{1}{2\pi\mu}\left[\int_{-a}^{a} \tau(\xi)n_1(y-\xi)d\xi + \mu\int_{-a}^{a} \phi(\xi)n_2(y-\xi)d\xi\right], \tag{9}$$

$$\sigma_z(y,0)|_{matrix} = -\frac{1}{2\pi}\left[\int_{-a}^{a} \tau(\xi)n_2(y-\xi)d\xi + \mu\int_{-a}^{a} \phi(\xi)n_3(y-\xi)d\xi\right], \tag{10}$$

where μ is the shear modulus of the host medium and $n_1(y)$, $n_2(y)$ and $n_3(y)$ are known functions given in Appendix B.

ϕ and τ can be determined from the continuity condition between the actuator and the host medium, given by

$$\varepsilon_y^a(y) = \varepsilon_y(y,0), \quad \sigma_z^a(y) = \sigma_z(y,0), \quad |y| < a, \tag{11}$$

where $\varepsilon_y(y,0)$, $\sigma_z(y,0)$ are the resulting dynamic fields in the host medium and the superscript "a" represents the actuator. Substituting (3), (6), (9) and (10) into (11), the continuity condition between the actuator and the host medium can be expressed in terms of integral equations as

$$-\frac{1}{2\pi\mu}\int_{-a}^{a}[\tau(\xi)n_1(y-\xi)+\mu\phi(\xi)n_2(y-\xi)]d\xi - \frac{\sin k_a(a+y)}{hE_a\sin 2k_a a}\int_{-a}^{a} p(\xi)\cos k_a(\xi-a)d\xi$$
$$+\frac{1}{hE_a}\int_{-a}^{y} p(\xi)\cos k_a(\xi-y)d\xi = \varepsilon_0(y), \quad |y| < a, \tag{12}$$

$$-\frac{1}{2\pi}\int_{-a}^{a}[\tau(\xi)n_2(y-\xi)+\mu\phi(\xi)n_3(y-\xi)]d\xi - \frac{c_{33}^a}{h}\int_{-a}^{y}\phi(\xi)d\xi$$
$$-\frac{c_{31}^a\sin k_a(a+y)}{hE_a\sin 2k_a a}\int_{-a}^{a}[\tau(\xi)+c_{31}^a\phi(\xi)]\cos k_a(\xi-a)d\xi$$
$$+\frac{c_{31}^a}{hE_a}\int_{-a}^{y}[\tau(\xi)+c_{31}^a\phi(\xi)]\cos k_a(\xi-y)d\xi$$
$$= c_{31}^a\varepsilon_0(y) - e_{33}^a E_z(y), \quad |y| < a \text{ embedded}. \tag{13}$$

Detailed evaluation of the kernels indicates that these equations are singular integral equations of the first kind, which involve a square-root singularity of τ and ϕ at the ends of the actuator. The general solution of τ and ϕ can be expressed in terms of Chebyshev polynomials as

$$\tau(y) = \sum_{j=0}^{\infty} A_j T_j(y/a)/\sqrt{1-y^2/a^2},$$
$$\phi(y) = \sum_{j=1}^{\infty} B_j T_j(y/a)/\sqrt{1-y^2/a^2} \tag{14}$$

with T_j being Chebyshev polynomials of the first kind and A_j and B_j being unknown constants to be determined.

If the expansions in Eq. (14) are truncated to the $(N-1)$th term and Eqs. (12) and (13) are satisfied at the following collocation points along the actuator:

$$y^l = a\cos\frac{l-1}{N-1}\pi, \quad l = 1,2,\ldots,N, \tag{15}$$

$2N$ linear algebraic equations in terms of A_j and B_j can be obtained, from which the unknown coefficient $\{c\} = \{A_0, A_1, \ldots, A_{N-1}, B_1, B_2, \ldots, B_{N-1}\}^T$ and τ and ϕ can be calculated.

2.2 Elastic wave propagation resulting from the actuator

The resulting elastodynamic field and the wave propagation in the host medium due to the actuator can be obtained in terms of $\{c\}$ as discussed in the previous subsection. By applying the inverse Fourier transform, the stress field in the host medium can be determined such that

$$\sigma_y(y,z) = -\frac{1}{k^2}\sum_{j=0}^{N} A_j \int_0^{\infty} H_1(s,z)P_j^1(s,y)ds - \frac{\mu}{k^2}\sum_{j=1}^{N} B_j \int_0^{\infty} H_2(s,z)P_j^1(s,y)ds, \tag{16}$$

$$\sigma_z(y,z) = -\frac{1}{k^2}\sum_{j=0}^{N} A_j \int_0^{\infty} H_3(s,z)P_j^1(s,y)ds - \frac{\mu}{k^2}\sum_{j=1}^{N} B_j \int_0^{\infty} H_4(s,z)P_j^1(s,y)ds, \tag{17}$$

$$\sigma_{yz}(y,z) = \frac{sgn(z)}{k^2}\sum_{j=0}^{N} A_j \int_0^{\infty} H_5(s,z)P_j^2(s,y)ds + \frac{sgn(z)\mu}{k^2}\sum_{j=1}^{N} B_j \int_0^{\infty} H_6(s,z)P_j^2(s,y)ds, \tag{18}$$

where $P_j^1(s,y)$, $P_j^2(s,y)$, $H_1(s,z)$, $H_2(s,z)$, $H_3(s,z)$, $H_4(s,z)$, $H_5(s,z)$ and $H_6(s,z)$ are known functions given in Appendix B.

The resulting elastic wave given by Eqs. (16)–(18) is very complicated. To evaluate the property of wave propagation, the asymptotic behavior of the wave at far-field is studied. A polar coordinate system (R,θ) will be used in the analysis, which is related to (y,z) by

$$y = R\cos\theta, \quad z = R\sin\theta \tag{19}$$

with the origin of the coordinate system being at the centre of the actuator. Let us consider the resulting $\sigma_y(y,z)$ in the host medium for the case involving a surface-bonded actuator. In the far-field, when $R \gg 1$, $\sigma_y(y,z)$ can be written as

$$\sigma_y^f(y,z) = \sum_{j=0}^{N} A_j \left\{ \int_{-\infty}^{\infty} \frac{2N_j^1 J_j(sa) s\beta(k^2+2\alpha^2) e^{-R(\alpha\sin\theta - is\cos\theta)}}{(2s^2-\beta^2)^2 - 4s^2\alpha\beta} ds \right.$$

$$\left. - \int_{-\infty}^{\infty} \frac{2N_j^1 J_j(sa)(2s^2-k^2) e^{-R(\beta\sin\theta - is\cos\theta)}}{(2s^2-\beta^2)^2 - 4s^2\alpha\beta} ds \right\}, \tag{20}$$

where J_j is the Bessel function of the first kind and

$$N_j^1 = \begin{cases} \dfrac{(-1)^n}{2} & j = 2n+1 \\ \dfrac{(-1)^{n+1}}{2i} & j = 2n, \end{cases} \tag{21}$$

where α and β are defined in Appendix B. It is well-known that $F(s) = (2s^2-\beta^2)^2 - 4s^2\alpha\beta$ will be zero at $s = +\omega/c_R,\ -\omega/c_R$ with c_R being the speed of the Rayleigh wave. As a result, the integrand has two singular points, which correspond to the Rayleigh wave propagating along the free surface. Since the Rayleigh wave will decay exponentially with the distance from the free surface, it will be ignored in the far-field solution.

The steepest descent approximation [22] is used to evaluate the far-field behavior of the stress field. For the integration given in Eq. (20), for a large R the dominant contribution to the integration comes from the vicinity of the saddle points of the exponents, which can be determined by $d(\alpha\sin\theta - is\cos\theta)/ds = 0$ and $d(\beta\sin\theta - is\cos\theta)/ds = 0$. This is because the real parts of the exponential functions are relatively small except in this area. The accuracy of this approximation improves with increasing R. For $\lambda_0(s) = \alpha\sin\theta - is\cos\theta$, the saddle point s_0 can be determined as $s_0 = K\cos\theta$. In applying the steepest descent approximation, the original path of integration is deformed to that along the path of steepest descent of $\lambda_0(s)$ running through its saddle point. Along the path of steepest descent $\lambda_0(s)$ can be expanded in a Taylor series

$$\lambda_0(s) = \lambda(s)|_{s=s_0} + \frac{1}{2}(s-s_0)^2\lambda''(s)|_{s=s_0} + \ldots \tag{22}$$

It can be proved that, along this path, the value of $\lambda_0(s) - \lambda(s)|_{s=s_0}$ will always be real and positive. Therefore, a real variable t_0 can be introduced as

$$\frac{1}{2}(s-s_0)^2\lambda_0''(s)|_{s=s_0} = t_0^2. \tag{23}$$

λ_0 can then be expressed as

$$\lambda_0(s) = \lambda(s)|_{s=s_0} + t_0^2. \tag{24}$$

Similarly, for the function $\lambda_1(s) = \beta\sin\theta - is\cos\theta$, the saddle point can be determined as $s_1 = k\cos\theta$, and λ_1 can be expressed along the path of steepest descent as

$$\lambda_1(s) = \lambda(s)|_{s=s_1} + t_1^2 \tag{25}$$

with t_1 being real and given by

$$\frac{1}{2}(s-s_1)^2\lambda_1''(s)|_{s=s_1} = t_1^2. \tag{26}$$

Substituting Eqs. (23) and (26) into Eq. (20), the integration can be reduced to

$$\sigma_y^f(y,z) = \sum_{j=0}^{N} A_j \left\{ F_j(s)|_{s=s_0} e^{-R\lambda_0(s)|_{s=s_0}} \int_{-\infty}^{\infty} e^{-Rt_0^2} \left(\frac{ds}{dt_0} \right) dt_0 \right\}$$

$$- \sum_{j=0}^{N} A_j \left\{ G_j(s)|_{s=s_1} e^{-R\lambda_1(s)|_{s=s_1}} \int_{-\infty}^{\infty} e^{-Rt_1^2} \left(\frac{ds}{dt_1} \right) dt_1 \right\}, \tag{27}$$

where

$$F_j(s) = \frac{2N_j^1 J_j(sa) s\beta(k^2 + 2\alpha^2)}{(2s^2 - \beta^2)^2 - 4s^2\alpha\beta}, \tag{28}$$

$$G_j(s) = \frac{2N_j^1 J_j(sa)(2s^2 - k^2)}{(2s^2 - \beta^2)^2 - 4s^2\alpha\beta}. \tag{29}$$

To calculate ds/dt_0 for the first integration in (27), the direction of the integral path in the s-plane should be determined. In general, s can be expressed as

$$s = s_0 + r_0 e^{i\theta_0}. \tag{30}$$

Since

$$\lambda_0''(s)|_{s=s_0} = \frac{1}{K \sin^2 \theta} e^{i\pi/2}, \tag{31}$$

from Eq. (23), t_0^2 can be expressed as

$$t_0^2 = \frac{1}{2} r_0^2 e^{2i\theta_0} \frac{1}{K \sin^2 \theta} e^{i\pi/2}. \tag{32}$$

Because t_0^2 is real, it can be concluded that

$$\theta_0 = -\pi/4, \quad r_0^2 = 2K \sin^2 \theta t_0^2. \tag{33}$$

Therefore,

$$\frac{ds}{dt_0} = \frac{dr_0}{dt_0} e^{-i\pi/4} = \sqrt{2K} \sin \theta e^{-i\pi/4}. \tag{34}$$

Similarly, ds/dt_1 in the second integration can be determined as

$$\frac{ds}{dt_1} = \sqrt{2k} \sin \theta e^{-i\pi/4}. \tag{35}$$

Making use of the following result:

$$\int_{-\infty}^{\infty} e^{-Rt^2} dt = \left(\frac{\pi}{R} \right)^{\frac{1}{2}}, \tag{36}$$

the analytical solution for the far-field elastic wave can be determined as

$$\sigma_y^f = \sum_{j=0}^{N} A_j \left[f_1(j,\theta) \sqrt{\frac{2\pi K}{R}} e^{i(KR - \frac{\pi}{4})} + f_2(j,\theta) \sqrt{\frac{2\pi k}{R}} e^{i(kR - \frac{\pi}{4})} \right] N_j^1$$

$$+ \sum_{j=1}^{N} B_j \left[f_3(j,\theta) \sqrt{\frac{2\pi K}{R}} e^{i(KR - \frac{\pi}{4})} + f_4(j,\theta) \sqrt{\frac{2\pi k}{R}} e^{i(kR - \frac{\pi}{4})} \right] N_j^1. \tag{37}$$

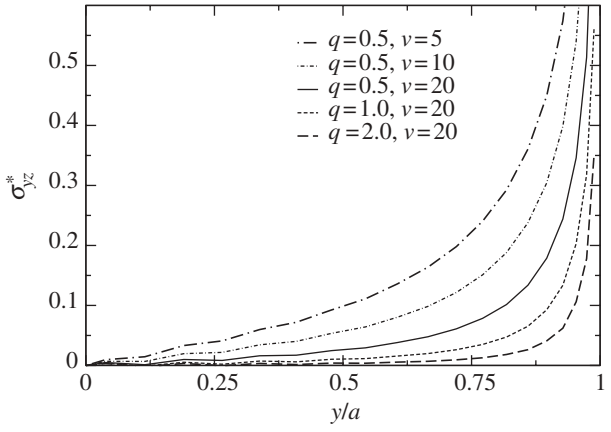

Fig. 3. Interfacial shear stress induced by a surface-bonded actuator

Similarly, the far-field solution of the stress components σ_z^f and σ_{yz}^f can be obtained as

$$\sigma_z^f = \sum_{j=0}^{N} A_j \left[f_5(j,\theta)\sqrt{\frac{2\pi K}{R}} e^{i(KR-\frac{\pi}{4})} + f_6(j,\theta)\sqrt{\frac{2\pi k}{R}} e^{i(kR-\frac{\pi}{4})} \right] N_j^1 + \sum_{j=1}^{N} B_j \left[f_7(j,\theta)\sqrt{\frac{2\pi K}{R}} e^{i(KR-\frac{\pi}{4})} + f_8(j,\theta)\sqrt{\frac{2\pi k}{R}} e^{i(kR-\frac{\pi}{4})} \right] N_j^1, \tag{38}$$

$$\sigma_{yz}^f = \sum_{j=0}^{N} A_j \left[f_9(j,\theta)\sqrt{\frac{2\pi K}{R}} e^{i(KR-\frac{\pi}{4})} + f_{10}(j,\theta)\sqrt{\frac{2\pi k}{R}} e^{i(kR-\frac{\pi}{4})} \right] N_j^2 + \sum_{j=1}^{N} B_j \left[f_{11}(j,\theta)\sqrt{\frac{2\pi K}{R}} e^{i(KR-\frac{\pi}{4})} + f_{12}(j,\theta)\sqrt{\frac{2\pi k}{R}} e^{i(kR-\frac{\pi}{4})} \right] N_j^2, \tag{39}$$

where

$$N_j^2 = \begin{cases} \dfrac{(-1)^n}{2i} & j = 2n+1 \\ \dfrac{(-1)^n}{2} & j = 2n \end{cases} \tag{40}$$

and the functions $f_i(j,\theta)$, $i = 1, \ldots, 12$ are known functions given in Appendix C.

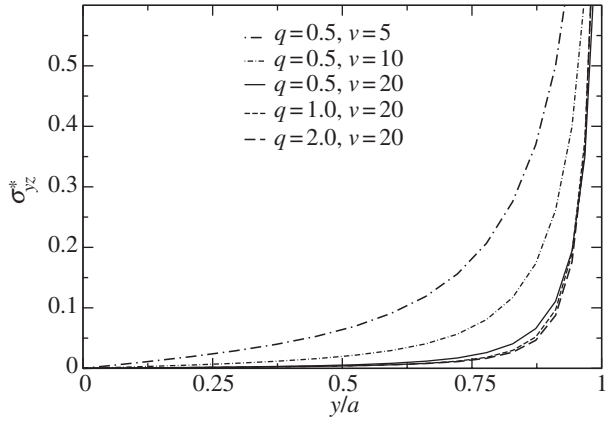

Fig. 4. Interfacial shear stress induced by an embedded actuator

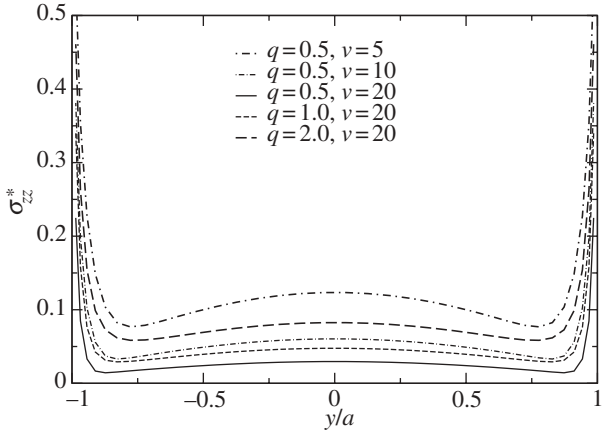

Fig. 5. Interfacial normal stress induced by an embedded actuator

For the special case that $y = 0$ and $z \longrightarrow \infty$, the following solution can be directly obtained:

$$\sigma_y^f = \sum_{j=0}^{N} A_j \left[\frac{W_1(j)}{|z|} e^{-iK_z} + \frac{W_2(j)}{|z|} e^{-ik_z} \right] - \mu \sum_{j=1}^{N} B_j \left[\frac{W_3(j)}{|z|} e^{-iK_z} - 2\frac{W_2(j)}{|z|} e^{-ik_z} \right], \tag{41}$$

$$\sigma_z^f = \sum_{j=0}^{N} A_j \left[\frac{W_4(j)}{|z|} e^{-iK_z} - \frac{W_2(j)}{|z|} e^{-ik_z} \right] - \mu \sum_{j=1}^{N} B_j \left[\frac{W_5(j)}{|z|} e^{-iK_z} - 2\frac{W_2(j)}{|z|} e^{-ik_z} \right], \tag{42}$$

$$\sigma_{yz}^f = \sum_{j=0}^{N} A_j \left[\frac{W_6(j)}{|z|} e^{-iK_z} - \frac{W_7(j)}{|z|} e^{-ik_z} \right] + \mu \sum_{j=1}^{N} B_j \left[\frac{W_8(j)}{|z|} e^{-iK_z} + \frac{W_9(j)}{|z|} e^{-ik_z} \right], \tag{43}$$

where $K_z = K|z|$, $k_z = k|z|$, and the constants $W_i(j)$, $i = 1, \ldots, 9$ are known functions given in Appendix C.

3 Results and discussion

This section is devoted to the discussion of the wave propagation induced by piezoelectric actuators bonded to and/or embedded in an elastic medium under different electric fields. In

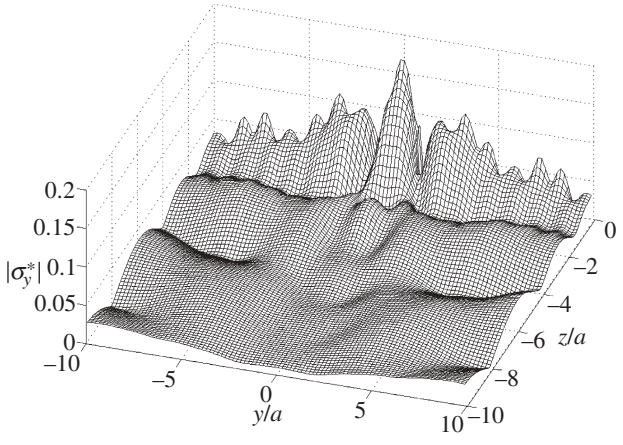

Fig. 6. The stress field induced by a surface-bonded actuator for $ka = 3.0$

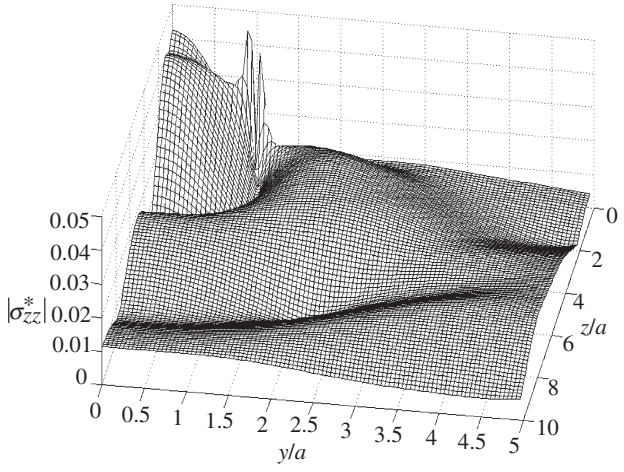

Fig. 7. The stress field induced by an embedded actuator for $ka = 3.0$

addition to the study of the influence of the geometry of the actuator, the material mismatch and the loading frequency, efforts are also made to determine the effect of the distribution of the applied electric field along the actuator upon the generated waveform.

The material constants of the actuator are assumed to be [23]

$$c_{11}^{(a)} = 13.9 \times 10^{10}(\text{Pa}), \quad c_{12}^{(a)} = 6.78 \times 10^{10}(\text{Pa}),$$

$$c_{13}^{(a)} = 7.43 \times 10^{10}(\text{Pa}), \quad c_{33}^{(a)} = 11.5 \times 10^{10}(\text{Pa}), \quad c_{44}^{(a)} = 2.56 \times 10^{10}(\text{Pa}),$$

$$e_{31}^{(a)} = -5.2(\text{C/m}^2), \quad e_{33}^{(a)} = 15.1(\text{C/m}^2), \quad e_{15}^{(a)} = 12.7(\text{C/m}^2),$$

$$\varepsilon_{11}^{(a)} = 6.45 \times 10^{-9}(\text{C/Vm}), \quad \varepsilon_{33}^{(a)} = 5.62 \times 10^{-9}(\text{C/Vm}),$$

$$\rho_a = 7500(\text{kg/m}^3).$$

3.1 Interfacial stresses

Wave propagation in the host medium generated by the actuator is governed by the interfacial shear and transverse stresses. Figure 3 shows the effect of the material mismatch $q = \pi\overline{E}/2E_a$, $\overline{E} = E/1 - v^2$, and the length-to-thickness ratio of the actuator $v = a/h$ upon the amplitude of

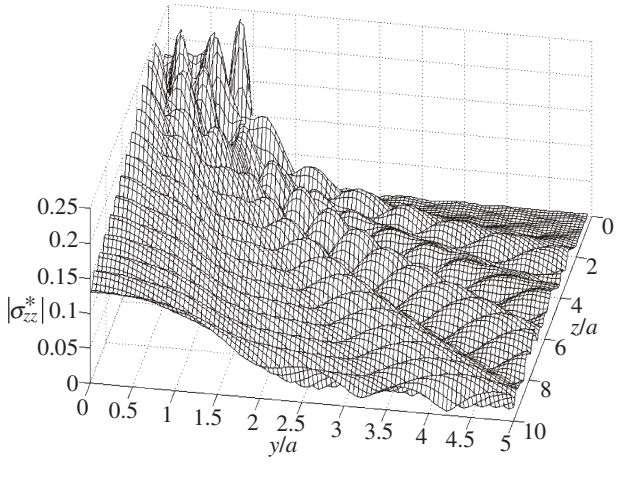

Fig. 8. The stress field induced by an embedded actuator for $ka = 20.0$

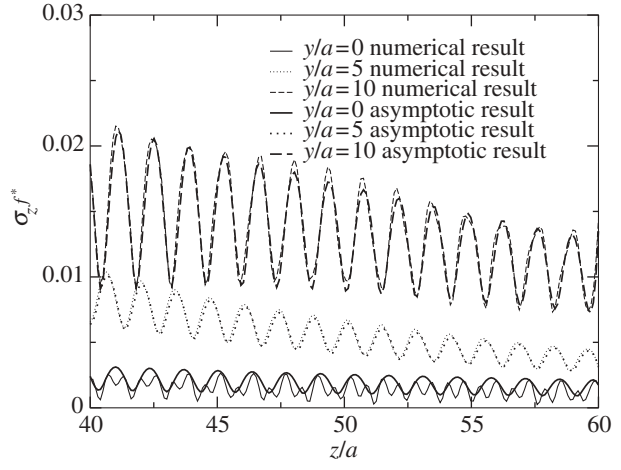

Fig. 9. The far-field stress induced by a surface-bonded actuator for $ka = 10.0$

the interfacial stress $\sigma_{yz}^* = \sigma_{yz}/\sigma_B$ of a surface-bonded actuator for the case where $ka = 2.0$ and $\rho_a/\rho_H = 1$, with $\sigma_B = e_a E_z$. The normalized interfacial shear stress increases with decreasing q and v. The result indicates that a shorter and/or stiffer actuator will generate relatively higher interfacial shear stress. In comparison, a longer and/or softer actuator will result in a shear stress distribution more concentrated at the tips.

Figures 4 and 5 show the effects of q and v upon the amplitude of the interfacial stresses $\sigma_{yz}^* = \sigma_{yz}/\sigma_B$ and $\sigma_z^* = \sigma_z/\sigma_B$ of an embedded actuator for the case where $ka = 2.0$ and $\rho_a/\rho_H = 1$. Similar results can be observed for the interfacial shear stress although the effect of q is not as significant as that for the surface-bonded actuator. The interfacial normal stress increases with increasing material mismatch q and decreasing length-to-thickness ratio v.

3.2 Complete wave field

The complete wave field in the host medium can be determined based on the interfacial stresses. Figure 6 shows the amplitude of the resulting elastic wave near a surface-bonded actuator under uniform electric fields, $\sigma_y^* = \sigma_y/\sigma_B$, for the case where $ka = 3.0$, $v = 20$, $q = 0.71$, and $\rho_a/\rho_H = 1$. Stress concentration can be observed around the tips of the actuator. The stresses reduce gradually with the distance from the actuator and eventually form a Rayleigh wave, which propagates with a constant amplitude along the surface of the host medium. Figure 7

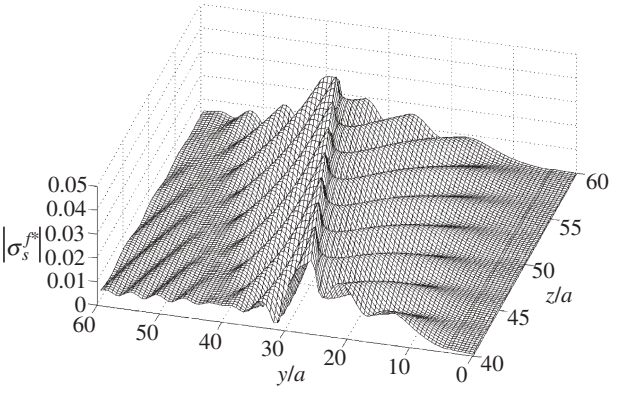

Fig. 10. The stress field induced by a surface-bonded actuator for $ka = 4.0$

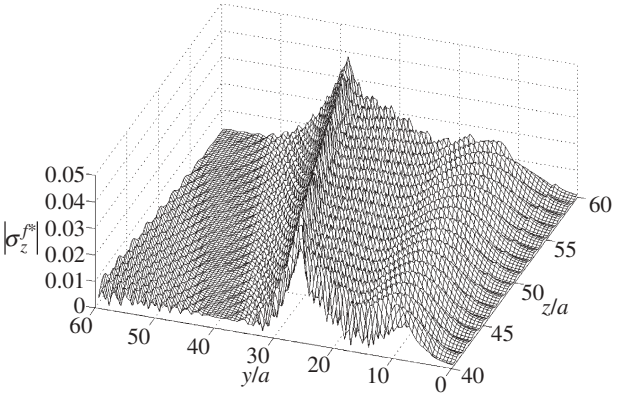

Fig. 11. The stress field induced by a surface-bonded actuator for $ka = 10.0$

shows the amplitude of $\sigma_z^* = \sigma_z/\sigma_B$ in the host medium caused by an embedded actuator under a uniform electric field for the case where $ka = 3.0$, $v = 20$, $q = 0.46$, and $\rho_a/\rho_H = 1$. In this case, recognizable wave propagation in both the axial and transverse directions can be observed. Figure 8 shows the amplitude of $\sigma_z^* = \sigma_z/\sigma_B$ in the host medium caused by the same embedded actuator discussed in Fig. 7 for higher frequency ($ka = 20$). A stronger wave propagation in the z-direction can be observed. This is caused by the higher transverse stress σ_z along the actuator-host interface due to the high loading frequency.

3.3 Far-field wave propagation

The analytical solution of the far-field wave propagation by the steepest descent approximation provided a clear description of the property of the generated wave propagation. In order to validate the accuracy of the obtained far-field solution, $\sigma_z^{f*} = \sigma_z^f/\sigma_B$ induced by a surface-bonded actuator determined by the asymptotic solution given in Eqs. (37)–(39) and (41)–(43) is compared in Fig. 9 with that of the complete solution using the integral equations (16)–(18) for the case where $ka = 10.0$, $q = 0.5$, $v = 20$ and $\rho_a/\rho_H = 1$. A uniform electric field is applied to the actuator. The very good agreement shows the high accuracy of the obtained asymptotic solution. Figures 10 and 11 show the far-field wave propagation induced by a surface-bonded actuator for the case where $q = 0.5$, $v = 20$ and $\rho_a/\rho_H = 1$, for loading frequencies $ka = 4$ and

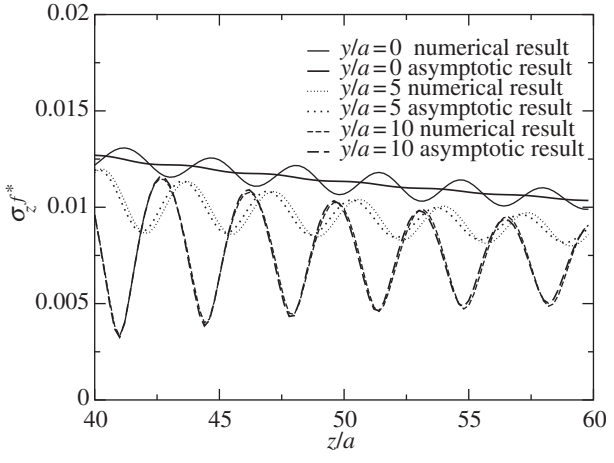

Fig. 12. The far-field stress induced by an embedded actuator for $ka = 4.0$

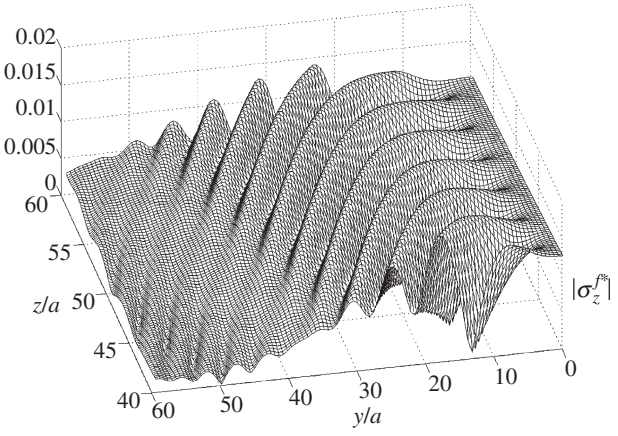

Fig. 13. The stress field induced by an embedded actuator for $ka = 4.0$

$ka = 10$, respectively. It can be found that the wave is mostly along the direction with $\theta = 25 - 30^\circ$ with respect to the z-axis.

Figure 12 shows the comparison of the stress $\sigma_z^{f*} = \sigma_z^f/\sigma_B$ induced by an embedded actuator predicted by the asymptotic solution with the stress by the complete solution for the case where $ka = 4.0$, $q = 0.5$, $v = 20$ and $\rho_a/\rho_H = 1$. Very good agreement is observed. Figure 13 shows the far-field wave propagation, σ_z^{f*}, for the case where $ka = 4.0$, $q = 0.5$, $v = 20$ and $\rho_a/\rho_H = 1$. In this case the wave propagates mainly along the z direction. Figure 14 shows the corresponding result for a higher frequency $ka = 10.0$. It is observed that the wave is now more focussed in the z-direction.

3.4 Wave propagation caused by electric fields with varying phases

In the above discussion, the actuator is excited by a uniformly applied electric field E_z. It is now well-understood that phased array actuators can generate specific waves propagating in desired directions by controlling the phase distribution among actuators. For the current problem, simulation is conducted to study whether thin-sheet actuators can generate wave propagation

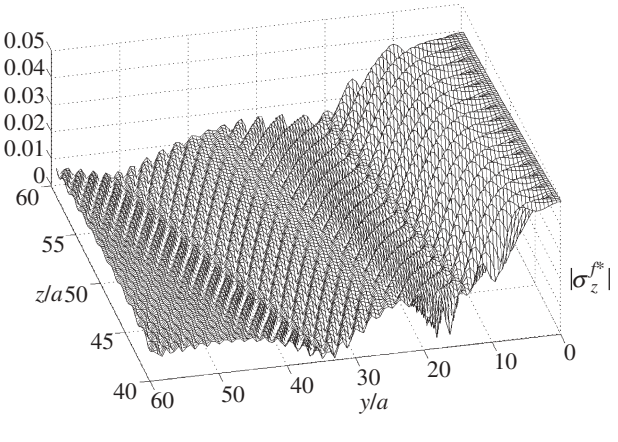

Fig. 14. The stress field induced by an embedded actuator for $ka = 10.0$

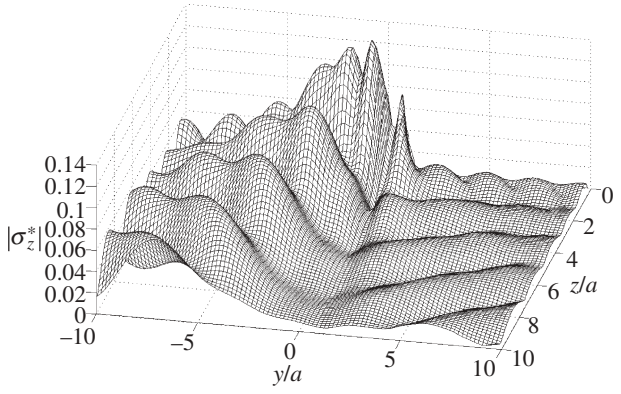

Fig. 15. Wave propagation induced by a surface-bonded actuator for $ka = 5.0$

in specific directions by controlling the phase distribution of the applied electric field. The electric field applied to the actuator is assumed to be

$$E_z(y) = E_z^0 e^{ik_a \sin\theta_s y},$$

where E_z^0 is the constant amplitude of the applied electric field, and θ_s is a steering angle.

Figure 15 shows the local wave field near a surface-bonded actuator caused by an electric field with varying phases for the case where $ka = 5.0$, $\theta_s = 30°$, $q = 0.5$, $v = 20$ and $\rho_a/\rho_H = 1$. It is interesting to observe that in this case the wave is the strongest along a specific direction. Figure 16 shows the corresponding local wave field near an embedded actuator for the case where $ka = 5.0$, $\theta_s = 30°$, $q = 0.5$, $v = 20$ and $\rho_a/\rho_H = 1$. Similar phenomena can be observed.

Figure 17 shows the far-field wave propagation by a surface-bonded actuator for different steering angles θ_s for the case where $ka = 10.0$, $q = 0.5$, $v = 20$ and $\rho_a/\rho_H = 1$. In frames (a)–(d), the steering angles are $\theta_s = 0°$, $30°$, $60°$, $90°$, respectively. Different wave fields can be obtained by changing the steering angle. For example, for $\theta_s = 0°$, the wave propagates mainly along $\theta = \pm 25°$ with respect to the z-axis. However, for $\theta_s = 30°$, the direction changes to $\theta = 20°$ with respect to the z-direction. For $\theta_s = 90°$, the direction of propagation is along $\theta = 25°$ with respect to the z-axis. Figure 18 shows the generated wave field far away from an embedded actuator with different steering angles θ_s for the case where

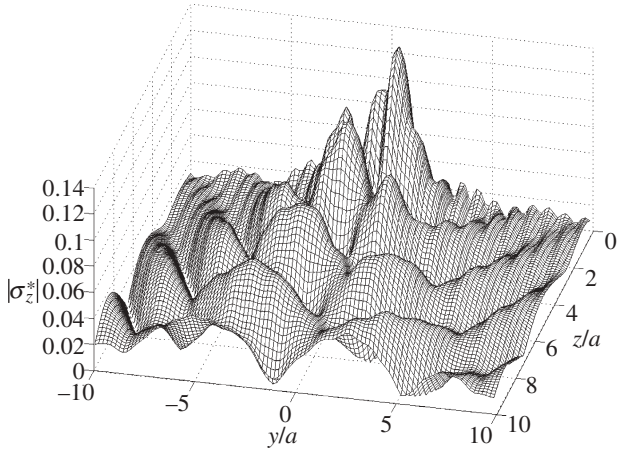

Fig. 16. Wave propagation induced by an embedded actuator for $ka = 5.0$

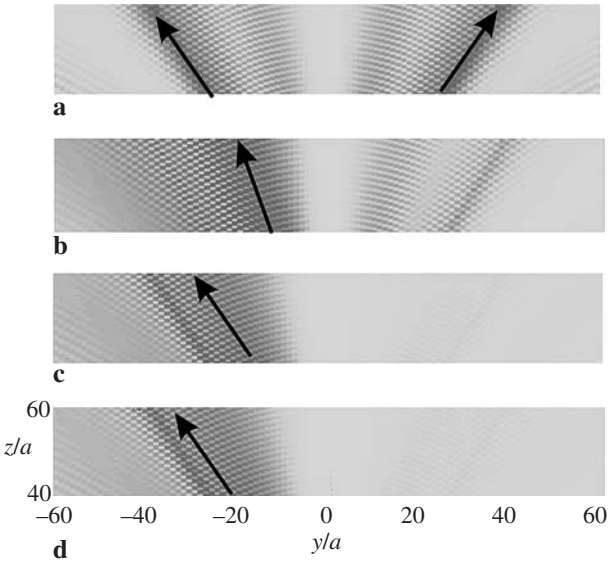

Fig. 17. Wave propagation induced by a surface-bonded actuator for $ka = 10.0$

$ka = 10.0$, $q = 0.5$, $v = 20$ and $\rho_a/\rho_H = 1$. Frames (a)–(d) correspond to $\theta_s = 0°$, $30°$, $60°$, $90°$, respectively.

4 Conclusions

An analytical solution and numerical simulation are provided to investigate the wave propagation induced by piezoelectric actuators surface-bonded to or embedded in an elastic medium under in-plane electric loads. The effect of the phase variation of the applied electric field along the actuator is considered. Based on the use of a one-dimensional actuator model, the dynamic

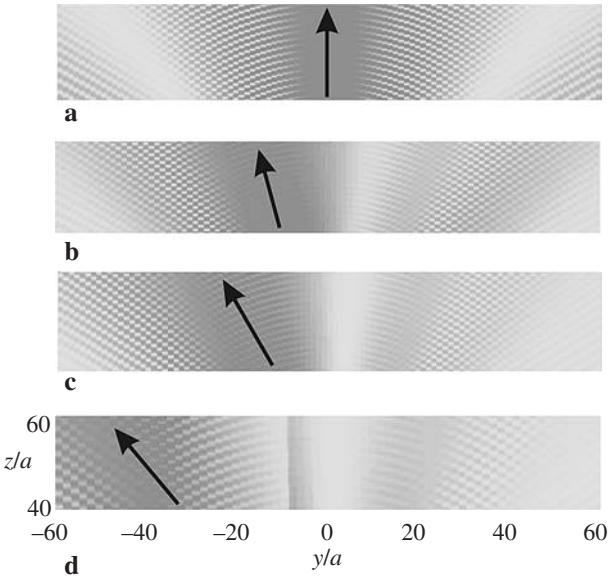

Fig. 18. Wave propagation induced by an embedded actuator for $ka = 10.0$

load transfer between the actuator and the host medium is studied. The steepest descent approximation is used to conduct the asymptotic analysis of the resulting wave field to identify the far-field waveform. The property of the resulting waveform is studied and the simulation shows that the direction of wave propagation can be adjusted by controlling the phase distribution of the applied electric field along the actuator.

Appendix A

Effective material constants

The electromechanical behavior of piezoelectric materials can be described by

$$\begin{Bmatrix} \sigma_x^a \\ \sigma_y^a \\ \sigma_z^a \\ \sigma_{yz}^a \\ \sigma_{xz}^a \\ \sigma_{xy}^a \end{Bmatrix} = \begin{bmatrix} c_{11}^a & c_{12}^a & c_{13}^a & 0 & 0 & 0 \\ c_{12}^a & c_{11}^a & c_{13}^a & 0 & 0 & 0 \\ c_{13}^a & c_{13}^a & c_{33}^a & 0 & 0 & 0 \\ 0 & 0 & 0 & c_{44}^a & 0 & 0 \\ 0 & 0 & 0 & 0 & c_{44}^a & 0 \\ 0 & 0 & 0 & 0 & 0 & c_{55}^a \end{bmatrix} \begin{Bmatrix} \varepsilon_x^a \\ \varepsilon_y^a \\ \varepsilon_z^a \\ 2\varepsilon_{yz}^a \\ 2\varepsilon_{xz}^a \\ 2\varepsilon_{xy}^a \end{Bmatrix} - \begin{bmatrix} 0 & 0 & e_{31}^a \\ 0 & 0 & e_{31}^a \\ 0 & 0 & e_{33}^a \\ 0 & e_{15}^a & 0 \\ e_{15}^a & 0 & 0 \\ 0 & 0 & 0 \end{bmatrix} \begin{Bmatrix} E_x \\ E_y \\ E_z \end{Bmatrix}$$

and

$$\begin{Bmatrix} D_x \\ D_y \\ D_z \end{Bmatrix} = \begin{bmatrix} 0 & 0 & e_{31}^a \\ 0 & 0 & e_{31}^a \\ 0 & 0 & e_{33}^a \\ 0 & e_{15}^a & 0 \\ e_{15}^a & 0 & 0 \\ 0 & 0 & 0 \end{bmatrix}^T \begin{Bmatrix} \varepsilon_x^a \\ \varepsilon_y^a \\ \varepsilon_z^a \\ 2\varepsilon_{yz}^a \\ 2\varepsilon_{xz}^a \\ 2\varepsilon_{xy}^a \end{Bmatrix} + \begin{bmatrix} \lambda_{11}^a & 0 & 0 \\ 0 & \lambda_{22}^a & 0 \\ 0 & 0 & \lambda_{33}^a \end{bmatrix} \begin{Bmatrix} E_x \\ E_y \\ E_z \end{Bmatrix},$$

where $c_{55}^a = (c_{11}^a - c_{12}^a)/2$ and the superscript "T" denotes the transpose of the matrix.

According to the current actuator model, the following condition should be satisfied under the plane strain deformation:

$$\varepsilon_x^a = 0.$$

For piezoelectric materials with their direction of polarization being along the z-axis, the stress component σ_y^a can be obtained, by substituting the above equations into the constitutive equation, as

$$\sigma_y^a = E_a \varepsilon_y^a + E_a' \varepsilon_z^a - e_a E_z,$$

where

$$E_a = \begin{cases} c_{11}^a & \text{embedded} \\ c_{11}^a - \dfrac{c_{13}^a}{c_{33}^a} & \text{surface-bonded,} \end{cases}$$

$$e_a = \begin{cases} e^a_{13} & \text{embedded} \\ e^a_{13} - e^a_{33}\dfrac{c^a_{13}}{c^a_{33}} & \text{surface-bonded,} \end{cases}$$

$$E'_a = \begin{cases} c^a_{13} & \text{embedded} \\ 0 & \text{surface-bonded.} \end{cases}$$

Appendix B

Useful functions in the integration

The kernels in integral equations (9) and (10) are

$$n_1(y-\xi) = \begin{cases} \frac{1}{k^2}\int_0^\infty \dfrac{s(s^2-\alpha\beta)}{\alpha}\sin s(\xi-y)ds & \text{embedded} \\ \int_0^\infty \dfrac{2k^2 s\beta}{(2s^2-k^2)^2 - 4s^2\alpha\beta}\sin s(\xi-y)d\xi & \text{surface-bonded,} \end{cases}$$

$$n_2(y-\xi) = \begin{cases} \frac{1}{k^2}\int_0^\infty \dfrac{s(-\gamma+2\alpha\beta)}{\alpha}\sin s(\xi-y)ds & \text{embedded} \\ 0 & \text{surface-bonded,} \end{cases}$$

$$n_3(y-\xi) = \begin{cases} \frac{1}{k^2}\int_0^\infty \dfrac{(\gamma^2-4s^2\alpha\beta)}{s\alpha}\sin s(\xi-y)ds & \text{embedded} \\ 0 & \text{surface-bonded,} \end{cases}$$

where $\gamma = s^2 + \beta^2$ and

$$\alpha = \begin{cases} \sqrt{s^2-K^2} & |s| > K \\ -i\sqrt{K^2-s^2} & |s| < K \end{cases} \qquad \beta = \begin{cases} \sqrt{s^2-k^2} & |s| > k \\ -i\sqrt{k^2-s^2} & |s| < k, \end{cases}$$

$K = \omega/c_L, \quad k = \omega/c_T,$

with c_L and c_T being the longitudinal and transverse shear wave velocities of the elastic medium, respectively.

The functions used in Eqs. (16)–(18) are given by

$$H_1(s,z) = \begin{cases} \dfrac{s(s^2+\beta^2)}{2\alpha}e^{-\alpha|z|} - s\beta e^{-\beta|z|} & \text{embedded} \\ \dfrac{2s\beta[(k^2+2\alpha^2)e^{-\alpha|z|} - (2s^2-k^2)e^{-\beta|z|}]}{(2s^2-\beta^2)^2 - 4s^2\alpha\beta} & \text{surface-bonded,} \end{cases}$$

$$H_2(s,z) = \begin{cases} -\dfrac{(2\alpha^2+k^2)(s^2+\beta^2)}{2\alpha s}e^{-\alpha|z|} + 2s\beta e^{-\beta|z|} & \text{embedded} \\ 0 & \text{surface-bonded,} \end{cases}$$

$$H_3(s,z) = \begin{cases} -\dfrac{s(s^2+\beta^2)}{2\alpha}e^{-\alpha|z|} + s\beta e^{-\beta|z|} & \text{embedded} \\ \dfrac{2s\beta(2s^2-k^2)(e^{-\alpha|z|} - e^{-\beta|z|})}{(2s^2-\beta^2)^2 - 4s^2\alpha\beta} & \text{surface-bonded,} \end{cases}$$

$$H_4(s,z) = \begin{cases} \dfrac{(s^2+\beta^2)^2}{2\alpha s}\, e^{-\alpha|z|} - 2s\beta e^{-\beta|z|} & \text{embedded} \\ 0 & \text{surfaced-bonded,} \end{cases}$$

$$H_5(s,z) = \begin{cases} s^2 e^{-\alpha|z|} - \dfrac{s^2+\beta^2}{2} e^{-\beta|z|} & \text{embedded} \\ \dfrac{4s^2\alpha\beta e^{-\alpha|z|} - (2s^2-k^2)e^{-\beta|z|}}{(2s^2-\beta^2)^2 - 4s^2\alpha\beta} & \text{surface-bonded,} \end{cases}$$

$$H_6(s,z) = \begin{cases} (s^2+\beta^2)(-e^{-\alpha|z|} + e^{-\beta|z|}) & \text{embedded} \\ 0 & \text{surface-bonded,} \end{cases}$$

and

$$P_j^1(s,y) = J_j(sa) \begin{cases} (-1)^{n+1}\sin(sy) & j = 2n \\ (-1)^n \cos(sy) & j = 2n+1, \end{cases}$$

$$P_j^2(s,y) = J_j(sa) \begin{cases} (-1)^n \sin(sy) & j = 2n+1 \\ (-1)^n \cos(sy) & j = 2n. \end{cases}$$

Appendix C

Functions for far-field stresses

The functions in the far-field solution in Eqs. (37)–(39) are given by

$$f_1(j,\theta) = \begin{cases} \dfrac{(k^2 - 2K^2\cos\theta^2)\sin\theta J_j(K\sin\theta)}{2} & \text{embedded} \\ \dfrac{g_1(j,\theta)}{m(\theta)} & \text{surface-bonded,} \end{cases}$$

$$f_2(j,\theta) = \begin{cases} k^2 \sin\theta\cos^2\theta J_j(k\sin\theta) & \text{embedded} \\ \dfrac{g_2(j,\theta)}{n(\theta)} & \text{surface-bonded,} \end{cases}$$

$$f_3(j,\theta) = \begin{cases} -\dfrac{(k^2 - 2K^2\cos^2\theta)(2K^2\sin\theta^2 - k^2)J_j(K\sin\theta)}{2K^2\sin\theta} & \text{embedded} \\ 0 & \text{surface-bonded,} \end{cases}$$

$$f_4(j,\theta) = \begin{cases} -2k^2\sin\theta\cos\theta^2 J_j(K\sin\theta) & \text{embedded} \\ 0 & \text{surface-bonded,} \end{cases}$$

$$f_5(j,\theta) = \begin{cases} \dfrac{(k^2 - 2K^2\cos^2\theta)\sin\theta J_j(K\sin\theta)}{2} & \text{embedded} \\ \dfrac{g_3(j,\theta)}{m(\theta)} & \text{surface-bonded,} \end{cases}$$

$$f_6(j,\theta) = \begin{cases} k^2 \sin\theta\cos^2\theta J_j(k\sin\theta) & \text{embedded} \\ \dfrac{g_2(j,\theta)}{n(\theta)} & \text{surface-bonded,} \end{cases}$$

$$f_7(j,\theta)=\begin{cases}\dfrac{(k^2-2K^2\sin^2\theta)^2J_j(K\sin\theta)}{2K^2\sin\theta} & \text{embedded}\\ 0 & \text{surface-bonded,}\end{cases}$$

$$f_8(j,\theta)=\begin{cases}2k^2\sin\theta\cos^2\theta J_j(k\sin\theta) & \text{embedded}\\ 0 & \text{surface-bonded,}\end{cases}$$

$$f_9(j,\theta)=\begin{cases}-iK^2\sin^2\theta\cos\theta J_j(K\sin\theta) & \text{embedded}\\ \dfrac{g_4(j,\theta)}{m(\theta)} & \text{surface-bonded,}\end{cases}$$

$$f_{10}(j,\theta)=\begin{cases}-\dfrac{i(2K^2\sin^2\theta-k^2)\cos\theta J_j(K\sin\theta)}{2} & \text{embedded}\\ \dfrac{g_5(j,\theta)}{n(\theta)} & \text{surface-bonded,}\end{cases}$$

$$f_{11}(j,\theta)=\begin{cases}-\dfrac{i(2K^2\sin^2\theta-k^2)\cos\theta J_j(K\sin\theta)}{2} & \text{embedded}\\ 0 & \text{surface-bonded,}\end{cases}$$

$$f_{12}(j,\theta)=\begin{cases}-i(2K^2\sin^2\theta-k^2)\cos\theta J_j(K\sin\theta) & \text{embedded}\\ 0 & \text{surface-bonded,}\end{cases}$$

with

$$m(\theta)=(2K^2\sin^2\theta-k^2)^2-4k^3\sin^2\theta|\cos\theta|\sqrt{k^2-K^2\sin^2\theta},$$

$$n(\theta)=(2K^2\sin^2\theta-k^2)^2+4ik^3\sin^2\theta|\cos\theta|\begin{cases}\sqrt{k^2\sin^2\theta-K^2} & k\sin\theta>K\\ (-i)\sqrt{K^2-k^2\sin^2\theta} & k\sin\theta<K,\end{cases}$$

$$g_1(j,\theta)=2KJ_j(K\sin\theta)\sin\theta|\cos\theta|\sqrt{k^2-K^2\sin^2\theta}(2K^2\sin^2\theta+k^2-K^2),$$

$$g_2(j,\theta)=2k^2J_j(k\sin\theta)\sin\theta\cos^2\theta(2k^2\sin^2\theta-K^2),$$

$$g_3(j,\theta)=-2KJ_j(K\sin\theta)\sin\theta|\cos\theta|\sqrt{k^2-K^2\sin^2\theta}(2K^2\sin^2\theta-k^2),$$

$$g_4(j,\theta)=4iK^3J_j(K\sin\theta)\sin^2\theta\cos^2\theta\sqrt{k^2-K^2\sin^2\theta},$$

$$g_5(j,\theta)=-iJ_j(k\sin\theta)|\cos\theta|(2k^2\sin^2\theta-k^2)^2.$$

The functions in Eqs. (41)–(43) are given by

$$W_1(j)=\begin{cases}\dfrac{J_j(K)(2K^2-k^2)}{2k^2}N_j^1 & \text{embedded}\\ \dfrac{-2N_j^1J_j(K)\sqrt{k^2-K^2}k^2K}{(2K^2-k^2)^2} & \text{surface-bonded,}\end{cases}$$

$$W_2(j)=\begin{cases}J_j(k)N_j^1 & \text{embedded}\\ 2N_j^1J_j(k), W_5(j)=N_j^2J_j(k) & \text{surface-bonded,}\end{cases}$$

$$W_3(j) = \frac{J_j(K)(2K^2 - k^2)^2}{2K^2k^2} N_j^1,$$

$$W_4(j) = \begin{cases} -J_j(K)N_j^1 & \text{embedded} \\ \frac{2N_j^1 J_j(K)\sqrt{k^2-K^2}k}{(2K^2-k^2)} & \text{surface-bonded,} \end{cases}$$

$$W_5(j) = \frac{J_j(K)(2K^2 - k^2)k^2}{K^2} N_j^1,$$

$$W_6(j) = \begin{cases} K^2 J_j(K)N_j^2 & \text{embedded} \\ \frac{2N_j^1 J_j(K)\sqrt{k^2-K^2}K}{(2K^2-k^2)} & \text{surface-bonded,} \end{cases}$$

$$W_7(j) = \begin{cases} (2K^2 - k^2)J_j(k)N_j^2/2 & \text{embedded} \\ \frac{4N_j^2 J_j(K)\sqrt{k^2-K^2}K^3}{(2K^2-k^2)^2} & \text{surface-bonded,} \end{cases}$$

$$W_8(j) = (2K^2 - k^2)J_j(K)N_j^2, \quad W_9(j) = (2K^2 - k^2)J_j(k)N_j^2.$$

Acknowledgement

This work was supported by the Natural Sciences and Engineering Research Council of Canada.

References

[1] Gandhi, M. V., Thompson, B. S.: Smart materials and structures. London: Chapman and Hall 1992.
[2] Chee, C., Tong, L., Steven, G. P.: A review on the modeling of piezoelectric sensors and actuators incorporated in intelligent structures. J. Intell. Mater. Syst. Struct. **9**, 3–19 (1998).
[3] Boller, C.: Next generation structural health monitoring and its integration into aircraft design. Int. J. Sys. Sci. **31**, 1333–1349 (2000).
[4] Bar-Cohen, Y.: Emerging NDE technologies and challenges at the beginning of the 3rd millennium – Part I. Material Evaluation **58**, 17–30 (2000).
[5] Crawley, E. F., de Luis, J.: Use of piezoelectric actuators as elements of intelligent structures. AIAA J. **25**, 1373–1385 (1987).
[6] Crawley, E. F., Anderson, E. H.: Detailed models of piezoelectric actuation of beams. J. Intell. Mater. Sys. Struct. **1**, 4–25 (1990).
[7] Lin, M. W., Rogers, C. A.: Actuation response of a beam structure with induced strain actuators. Adaptive Struct. Mater. Sys. **35**, 129–139 (1993).
[8] Dimitriadis, E. K., Fuller, C. R., Rogers, C. A.: Piezoelectric actuators for distributed noise and vibration excitation of thin plates. ASME J. Vibr. Acoust. **13**, 100–107 (1991).
[9] Tzou, H. S., Tseng, C. I.: Distributed vibration control and identification of coupled elastic/piezoelectric systems. Mech. Sys. Signal Proc. **5**, 215–231 (1991).
[10] Mitchell, J. A., Reddy, J. N.: A study of embedded piezoelectric layers in composite cylinders. ASME J. Appl. Mech. **62**, 166–173 (1995).
[11] Banks, H. T., Smith, R. C.: The modelling of piezoceramic patch interactions with shells, plates, and beams. Qu. Appl. Math. **53**, 353–381 (1995).
[12] Han, J. H., Lee, I.: Analysis of composite plates with piezoelectric actuators for vibration control using layerwise displacement theory. Composites, Part B **29**, 519–672 (1998).

[13] Wang, X. D., Meguid, S. A.: On the electroelastic behavior of a thin piezoelectric actuator attached to an infinite host structure. Int. J. Solids Struct. **37**, 3231–3251 (2000).
[14] Zhang, J. Q., Zhang B. N., Fan J. H.: A coupled electromechanical analysis of a piezoelectric layer bonded to an elastic substrate: Part I, development of governing equations. Int. J. Solids Struct. **40**, 6781–6797 (2003).
[15] Zhang B. N., Zhang, J. Q., Fan J. H.: A coupled electromechanical analysis of a piezoelectric layer bonded to an elastic substrate: Part II, numerical solution and applications. Int. J. Solids Struct. **40**, 6799–6612 (2003).
[16] Choi K. Y., Chang F. K.: Identification of foreign object impact in structures using distributed sensors. J. Intell. Mater. Sys. Struct. **5**, 864–869 (1994).
[17] Giurgiutiu, V., Rogers, C. A.: Modeling of the electro-mechanical (E/M) impedance response of a damaged composite beam. Adaptive Struct. Mater. Sys. **59**, 39–46 (1999).
[18] Giurgiutiu, V., Zagrai, A., Bao, J.: Embedded active sensors for in-situ structural health monitoring of thin-wall structures. ASME J. Pressure Vessel Techn. **124**, 134–145 (2002).
[19] Wang, X. D.: Coupled electromechanical behavior of piezoelectric actuators in smart structures. J. Intell. Mater. Sys. Struct. **10**, 232–241 (1999).
[20] Wang X. D., Huang G. L.: Wave propagation in electromechanical structures: induced by surface-bonded piezoelectric actuators. J. Intell. Mater. Sys. Struct. **12**, 105–115 (2001).
[21] Wang X. D., Huang G. L.: Wave propagation in electromechanical structures: induced by embedded piezoelectric actuators. J. Intell. Mater. Sys. Struct. **12**, 117–125 (2001).
[22] Achenbach, J. D.: Wave propagation in elastic solids. Amsterdam: North-Holland 1973.
[23] Park, S., Sun, C. T.: Fracture criteria for piezoelectric creamics. J. Amer. Ceramics Soc. **78**, 145–1480 (1995).

Authors' address: X. D. Wang and G. L. Huang, Department of Mechanical Engineering, University of Alberta, Edmonton, Alberta, Canada T6G 2G8 (E-mail: xiaodong.wang@ualberta.ca)